Supplementary Information

Electrically Modulated Plasmonic Metasurfaces for Light Communication

Xinyu Wen[1,2,3,4], Hongquan Yu[2,3,4], Yangjiang Wu[2,3,4], Erwei Gui[2,3,4,5], Shuyi Chen[1,4], Junhua Tang[1,2,3,4,6], Qinglin Ji[1,2,3], Peng Zhou[1,2,3,4,7], Boxiang Wang[2,3,4,8], Fanying Meng[1,4], Kaihuan Zhang[2,3,4,8], and Shikai Deng[1,2,3,4,8*]

[1]State Key Laboratory of Materials for Integrated Circuits, Shanghai Institute of Microsystem and Information Technology, Chinese Academy of Sciences, Shanghai 200050, China

[2]State Key Laboratory of Transducer Technology, Shanghai Institute of Microsystem and Information Technology, Chinese Academy of Sciences, Shanghai 200050, China

[3]2020 X-Lab, Shanghai Institute of Microsystem and Information Technology, Chinese Academy of Sciences, Shanghai 200050, China

[4]School of Graduate Study, University of Chinese Academy of Sciences, Beijing 100049, China

[5]Institute of Engineering Thermophysics, School of Mechanical Engineering, Shanghai Jiao Tong University, Shanghai 200240, China

[6]School of Mechanical and Power Engineering, East China University of Science and Technology, Shanghai, 200237, China

[7]State Key Laboratory of Information Photonics and Optical Communications, Beijing University of Posts and Telecommunications, Beijing 100876, China

[8]Center of Materials Science and Optoelectronics Engineering, University of Chinese Academy of Sciences, Beijing, 100049 China

* **Corresponding author:** sdeng@mail.sim.ac.cn

Table of contents

Summarized device performance of electrically modulated metasurfaces

Table S1. Summarized device performance of electrically modulated metasurfaces

Materials	Wavelength (nm)	Linewidths (nm)	Operation Voltages (V)	Tuning Sensitivity (nm/V)	Modulation Depth	Modulation Speed	Ref.
Phase change material	1320	~200	15.7	-	-	-	[28]
Phase change materials	1430	266	20	8.75	400%	-	[30]
Organic materials	1480	~ 22	80	0.06875	37%	50MHz	[34]
Organic materials	1550	~ 50	60	0.1	67%	GHz	[35]
Organic materials	1500	~ 33	100	0.015	11%	GHz	[36]
Organic materials	1495	~ 5	17	0.16	-	MHz	[37]
Silicon	780	20	4	3.5	90%	100Hz	[38]
Lithium Niobate	968.5	~2	10	0.019	4.2%	kHz	[39]
Liquid crystals	1600	76	70	0.71	700%	-	[41]
Lithium Niobate	1550	26	20	0.07	40%	500 Hz	[42]
Graphene	6500	2000	10	10	100%	20 GHz	[43]
Organic materials	1630	32	10	0.05	0.8%	5 MHz	[44]
Lithium Niobate	1560	1	24	0.011	-	30 GHz	[45]
Liquid crystals	669	30	20	0.3	53%	-	[46]
Phase-change materials	1340	~ 0.1	7.5	0.05	-	-	[47]
DMSO and ITO	550-800	10	Below 5	~1	43%	Hz	This work

Fabrication of electrically modulated metasurfaces

Ag NP lattices and Al NP lattices on TCO-quartz substrates were fabricated using a nanofabrication process that combines sputter deposition, electron-beam deposition, modified solvent-assisted nanoimprint embossing (SANE), and etching[1]. First, a 150 nm TCO layer is deposited by sputtering, and then the Al film or Ag film is deposited by electron beam evaporation, followed by photoresist (PR) S1805 spin-coated on the metal surface at 4000 rpm with an acceleration of 500 rpm/s for 30s. Nanoimprinting is performed on the photoresist to generate periodic PR columns with controlled size and period. The polydimethylsiloxane (PDMS) mask was rinsed with alcohol and then immersed in dimethylformamide (DMF) solution for 90 seconds. After drying with a nitrogen gun, it was pressed onto the sample coated with S1805 and left to stand for 1.5 hours before being removed. Metal NP lattices are formed by ion beam etching (IBE) and removing the PR with acetone. We performed IBE etching using the HAASRODE-I200 etcher from Leuven Instruments. The etching gas Ar flow rate is 24 sccm, with an etching angle of 0 degree, a temperature of 7 °C, and a voltage of 400V. The etching times for Al and Ag are 300 seconds and 96 seconds, respectively. Finally, the Au electrodes were deposited via electron beam evaporation with a hard mask to protect the metal NP array.

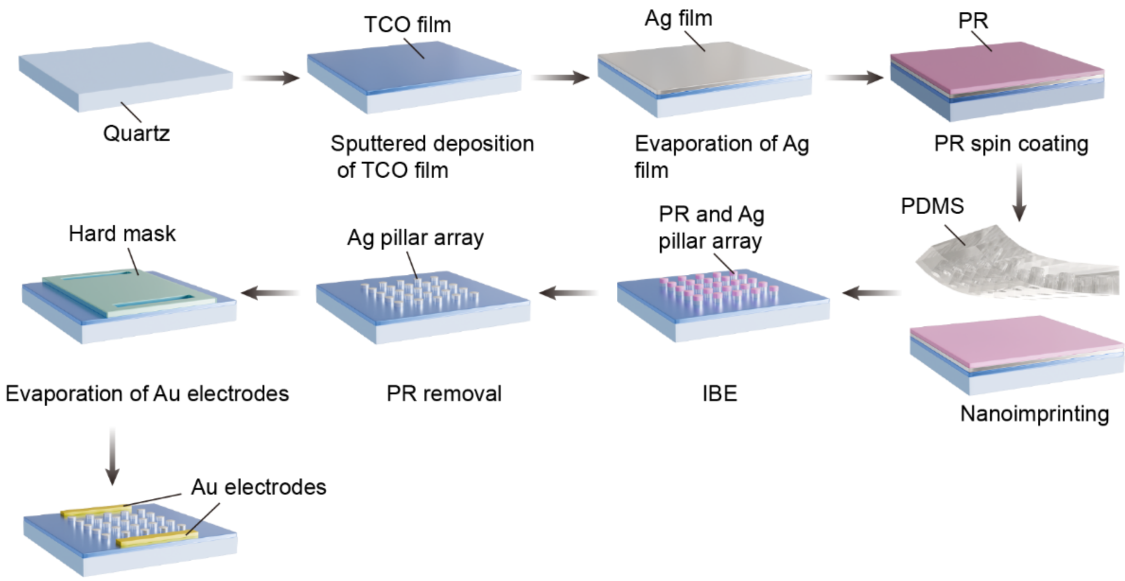

Figure S1. Fabrication of electrically modulated metasurface.

Refractive indices of ITO and ITGZO

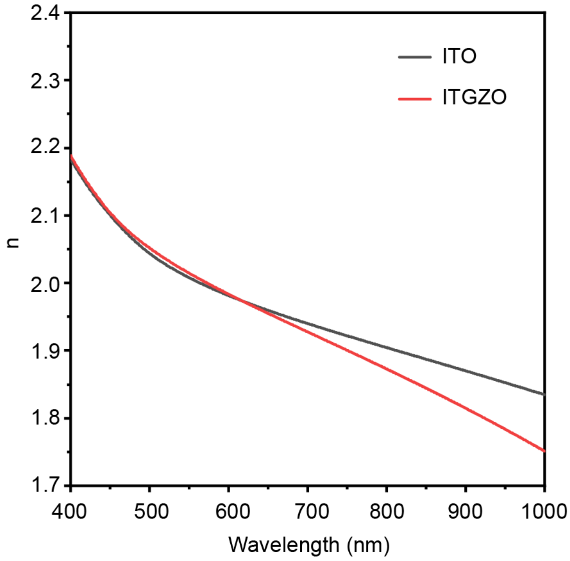

Figure S2. Refractive indices of ITO and ITGZO from 400 nm to 1000 nm measured by spectroscopic ellipsometry.

Resonance mode analysis of Ag and Al metasurfaces by the FDTD simulation

Finite-Difference-Time-Domain (FDTD) calculations were performed to simulate the optical responses of Ag NPs lattices and Al NPs lattices on the TCO layer. Optical constants for Ag and Al were taken from Palik measurements (400-1000 nm). These calculations used a uniform lattice size of 4 nm (x, y, and z).

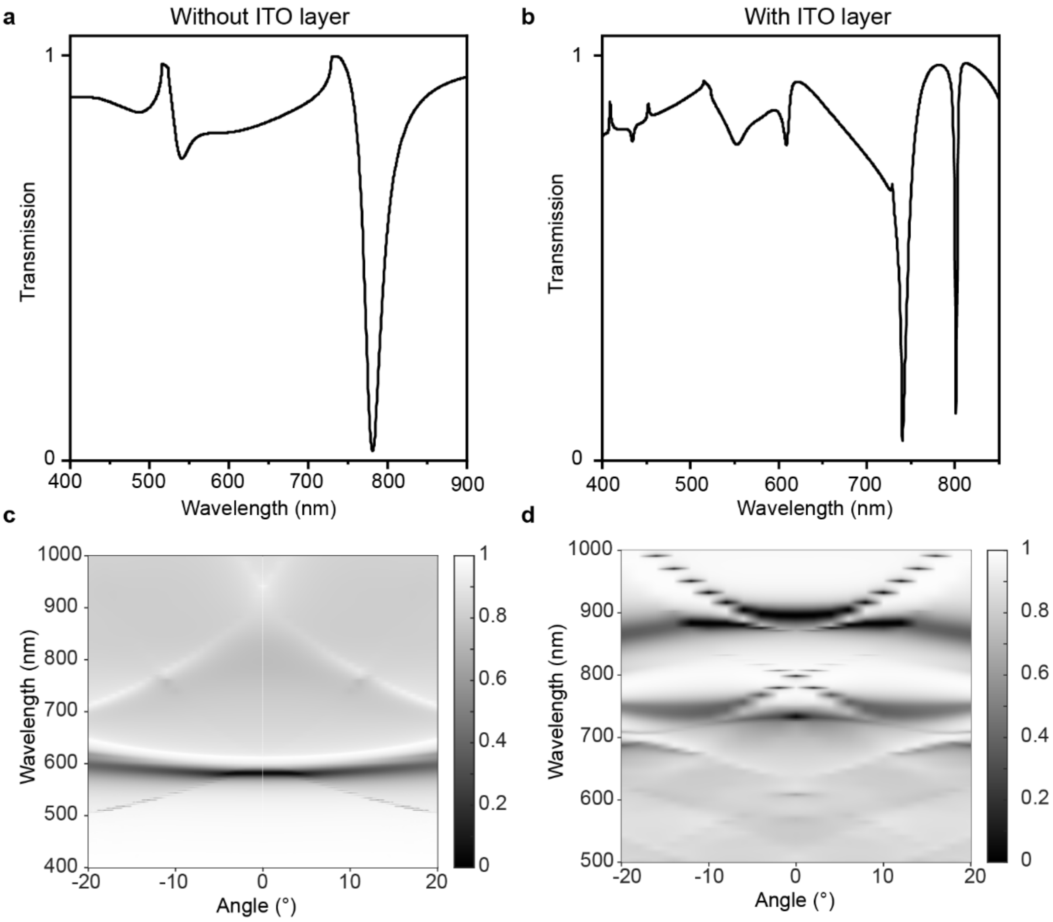

Figure S3. Simulated transmission spectra and dispersion of the Ag metasurface with and without the ITO layer. Transmission spectra of Ag metasurface **(a)** without ITO layer and **(b)** with ITO layer. Dispersion of Ag metasurface **(c)** without ITO layer and **(d)** with ITO layer.

We simulated the transmission spectra and dispersion of Ag NP lattices, both with and without the ITO layer, using the FDTD method to illustrate the function of the ITO layer. The period of the Ag NP lattices is 500 nm, the diameter is 130 nm, the height is 80 nm, and the thickness of the ITO layer is 150 nm. Ag metasurface without ITO layer exhibits a single SLR mode at 780 nm, while Ag metasurface with ITO layer exhibits multimodes at 740 nm and 801 nm due to the waveguide modes generated by the high refractive index ITO layer coupled with SLRs[2].

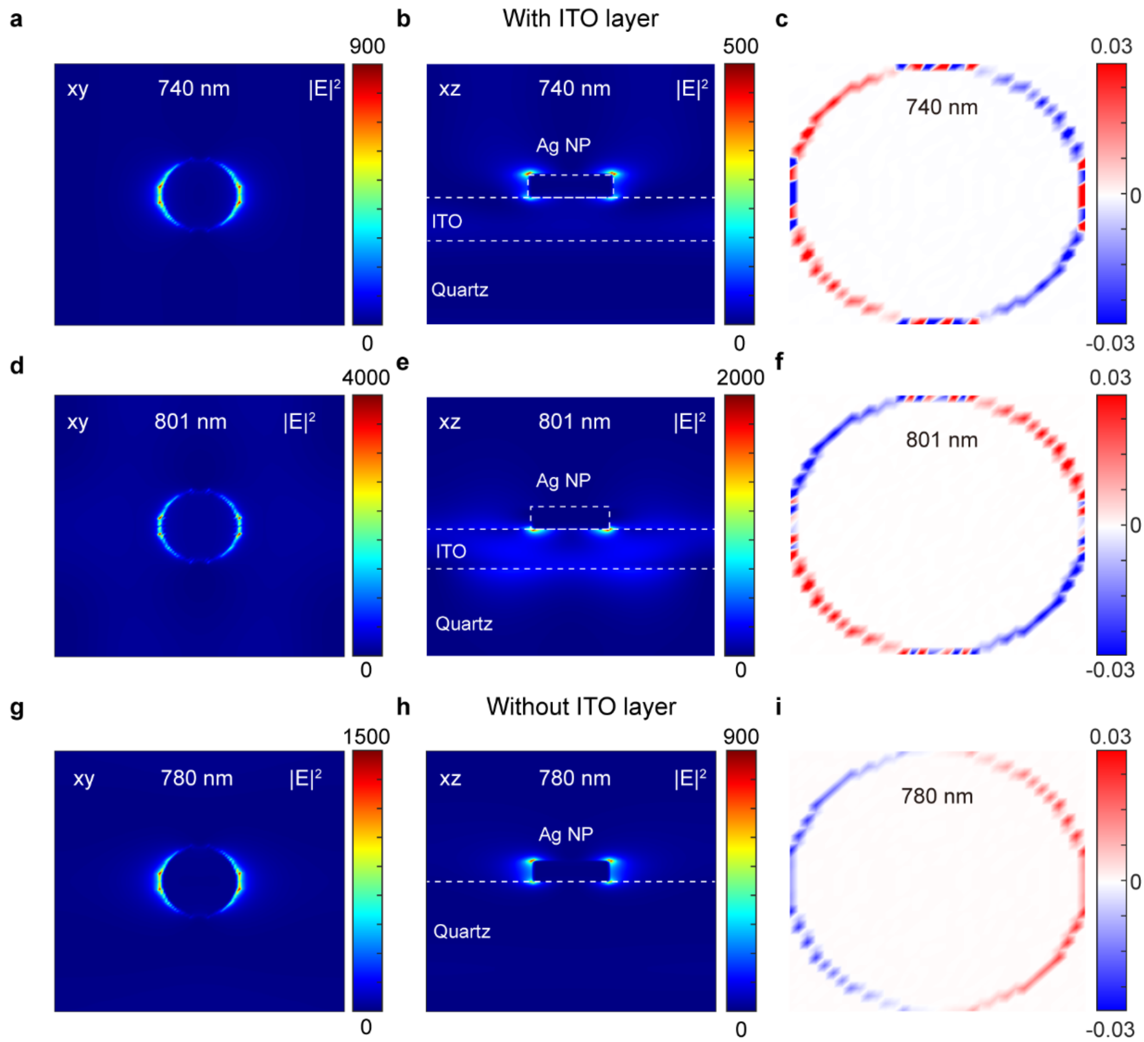

Figure S4. Simulated near fields and charge distributions of Ag NP lattices at different modes with and without the ITO layer. (a-f) Nearfield and charge distribution of two modes of Ag metasurface with the ITO layer. **(g-i)** Nearfield and charge distribution of Ag metasurface without the ITO layer.

The hot spots of the Ag metasurface without ITO layers are mainly concentrated on the upper and lower surfaces of the Ag NP, with a near-field enhancement of ~1500. We focus on two modes of Ag metasurface with the ITO layer: Mode 1 at 740 nm and Mode 2 at 801 nm. The hotspot of Mode 1 is mainly located on the upper surface of Ag, exhibiting a near-field enhancement of ~ 900, whereas the hotspot of Mode 2 is primarily situated at the interface between Ag NPs and the ITO layer, showing a near-field enhancement of ~ 4000. Single mode without ITO layer exhibits dipole charge distributions, while mode 2 displays an in-plane quadrupole charge distribution with the ITO layer.

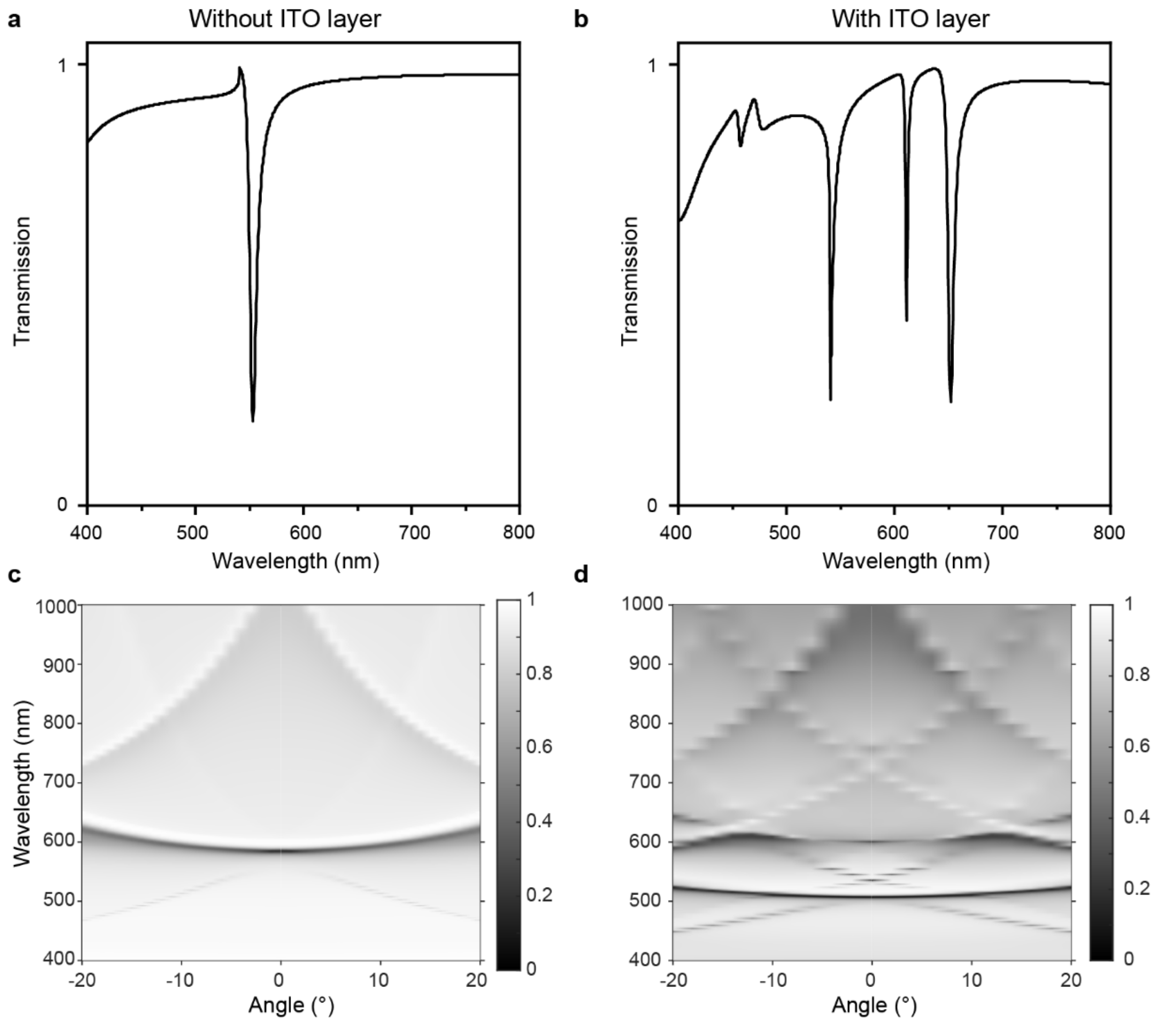

Figure S5. Simulated transmission spectra and dispersion of the Al metasurface with and without the ITO layer. Transmission spectra of Al NP lattices **(a)** without ITO layer, and **(b)** with ITO layer. Dispersion of Al NP lattices **(c)** without ITO layer, and **(d)** with ITO layer.

The period of the Al NP lattices is 370 nm, the diameter is 80 nm, the height is 80 nm, and the thickness of the ITO layer is 150 nm. An Al metasurface without an ITO layer exhibits a single SLR mode at 553 nm, while an Ag metasurface with an ITO layer exhibits multimodes at 541 nm, 611 nm, and 653 nm due to the waveguide modes generated by the high refractive index ITO layer coupled with SLR.

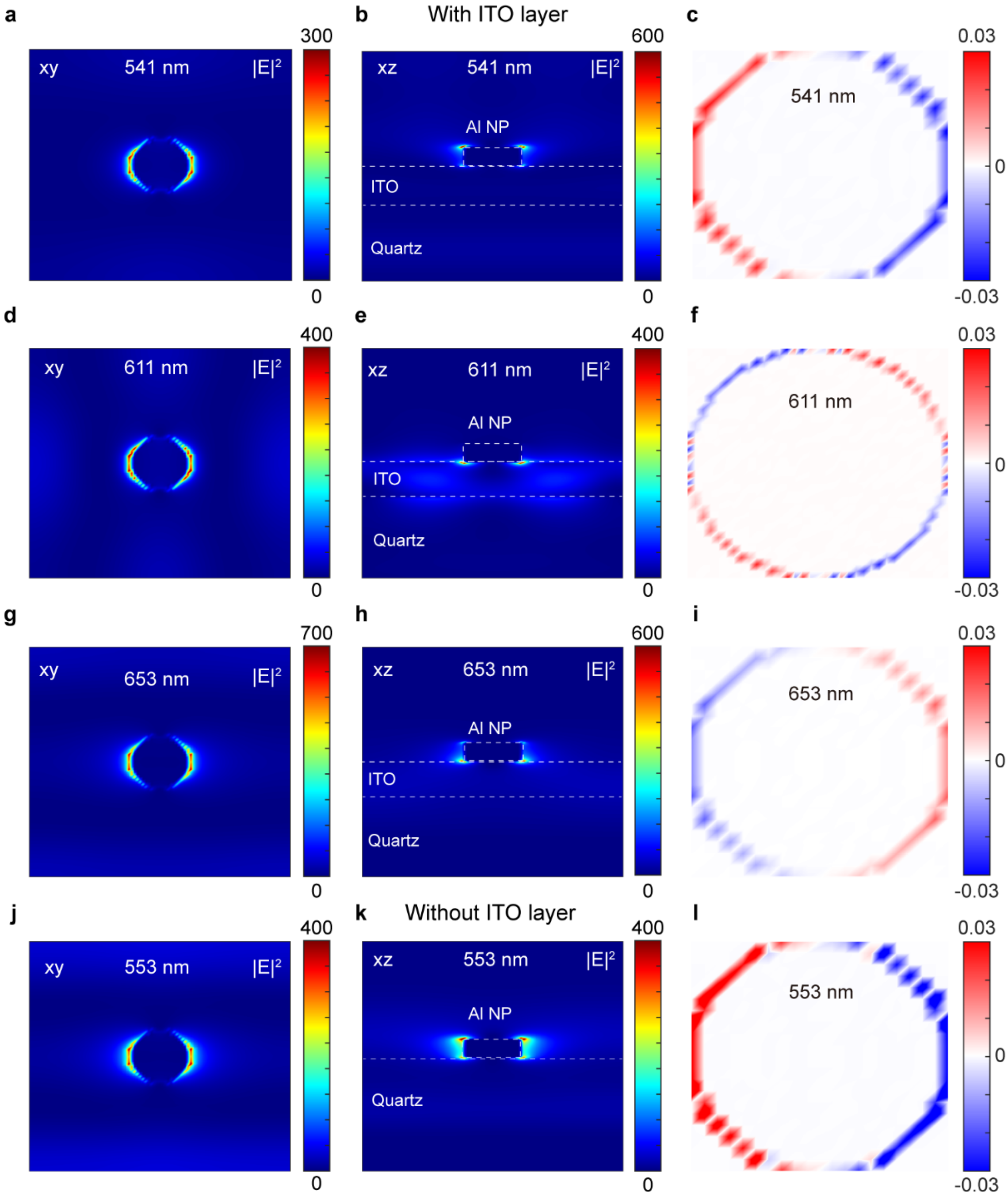

Figure S6. Simulated nearfield and charge distribution of Al NP lattices at different modes with and without the ITO layer. (a-i) Nearfield and charge distribution of Al NP lattices at 3 modes with the ITO layer. **(j-l)** Nearfield and charge distribution of Al NP lattices without the ITO layer.

The hot spots of the Al metasurface without ITO layers are mainly concentrated on the upper and lower surfaces of the Al NP, with a near-field enhancement of ~400. We concentrate on three modes of Al metasurface with the ITO layer: Mode 1 at 541 nm, Mode 2 at 611 nm, and Mode 3 at 653 nm. The hotspot of Mode 1 is mainly located on the upper surface of Al NP, with a near-field enhancement of ~ 600, while the hotspots of Mode 2 and mode 3 are primarily positioned at the interface between Ag NPs and the ITO layer, with a near-field enhancement of ~ 400 and ~700, respectively. Mode 2 exhibits an in-plane quadruple, while mode 1, mode 3, and the single mode without the ITO layer show in-plane dipole charge distribution.

Temperature distribution of the Ag metasurface at different voltages measured by the infrared thermal imaging camera

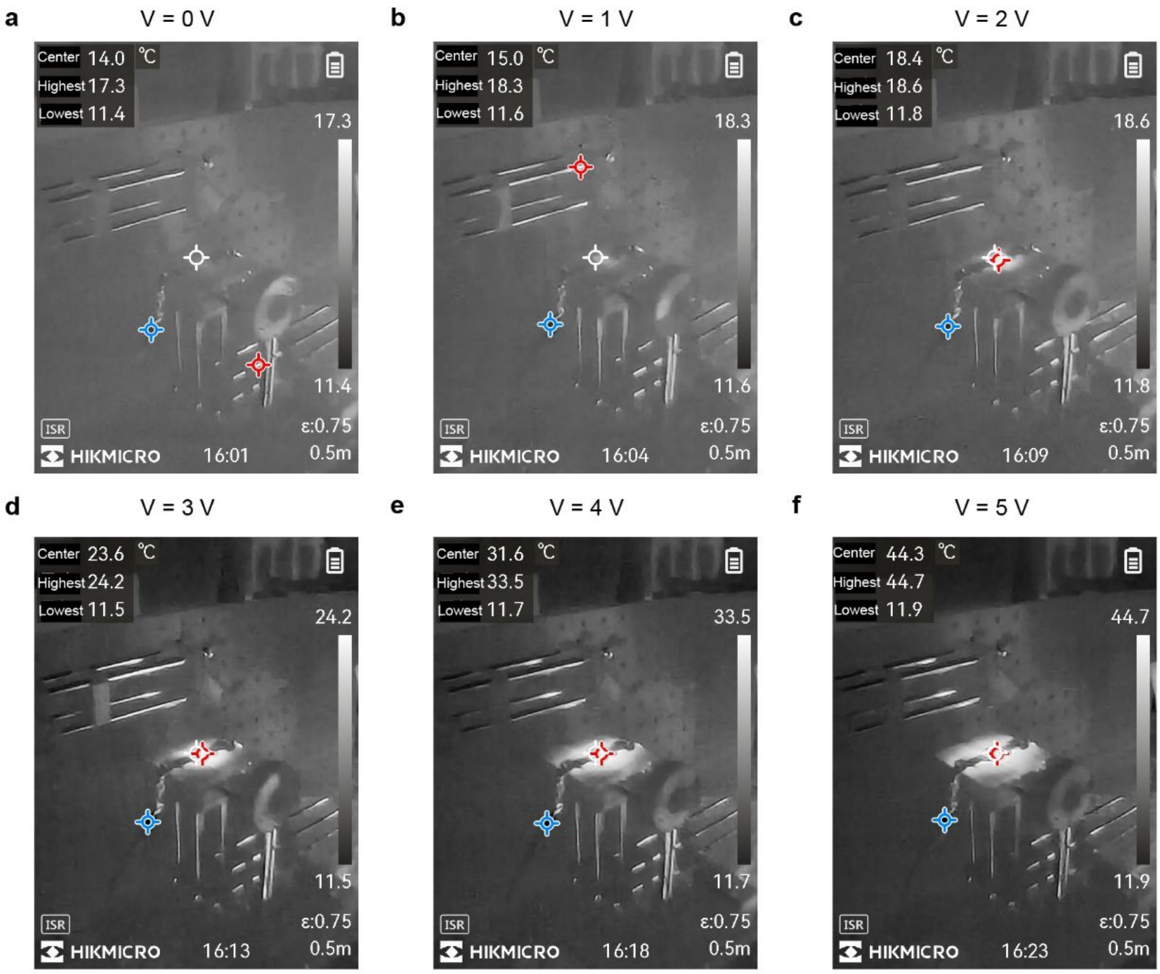

Figure S7. Temperature distribution of the Ag metasurface at different voltages. The white circle indicates the location of the sample, the blue circle indicates the area with the lowest temperature, and the red circle indicates the area with the highest temperature.

Simulated temperature distribution of the sample on different substrates

We simulate the temperature distribution of the device at different voltages by using the current module with the solid-state heat transfer module in COMSOL. The model is founded on the experimental setup employed for characterizing the modulation performance, with the dimensions of the metasurface in the model aligned to those of the experimental samples, as illustrated in **Figure S6a**. The samples are positioned on a plastic plate featuring a central aperture. It is worth noting that since the size of Al NPs and ITO relative to the overall size is very small, it makes it impossible to establish precise gridding. Consequently, these layers are simplified to a thermally thin layer for the heat transfer analysis. In the current study section, the conductivity of the Al is set as the contact impedance, while the thickness and the conductivity of the ITO are determined by the electrical shielding. This approach overlooks mesh accuracy concerns and yields a highly precise model. We simulated the temperature distribution of the samples positioned on the experimental characterization platform, on foam, and in air at varying voltages.

In the sample on the plastic plate, the material within the plastic holes of the test platform is designed as air, thereby establishing heat conduction in the plastic and the holes. The boundary conditions at the bottom of the air column and the bottom of the plastic are set as natural convection boundary conditions. For the sample on the foam, periodic boundary conditions are used around the foam, and natural convective boundary conditions are applied to the bottom of the foam substrate. Natural convective boundary conditions of $T_{e0} = 273 + 15K$ are used around and above the quartz. The electrical boundary conditions for all three models are electrically insulating due to the substrate approximation of the insulator. The area of the gold electrode without thickness was set as the input of the current, and the temperature distribution of the sample at different voltages was obtained by parameter scanning for voltages from 0 V to 5 V.

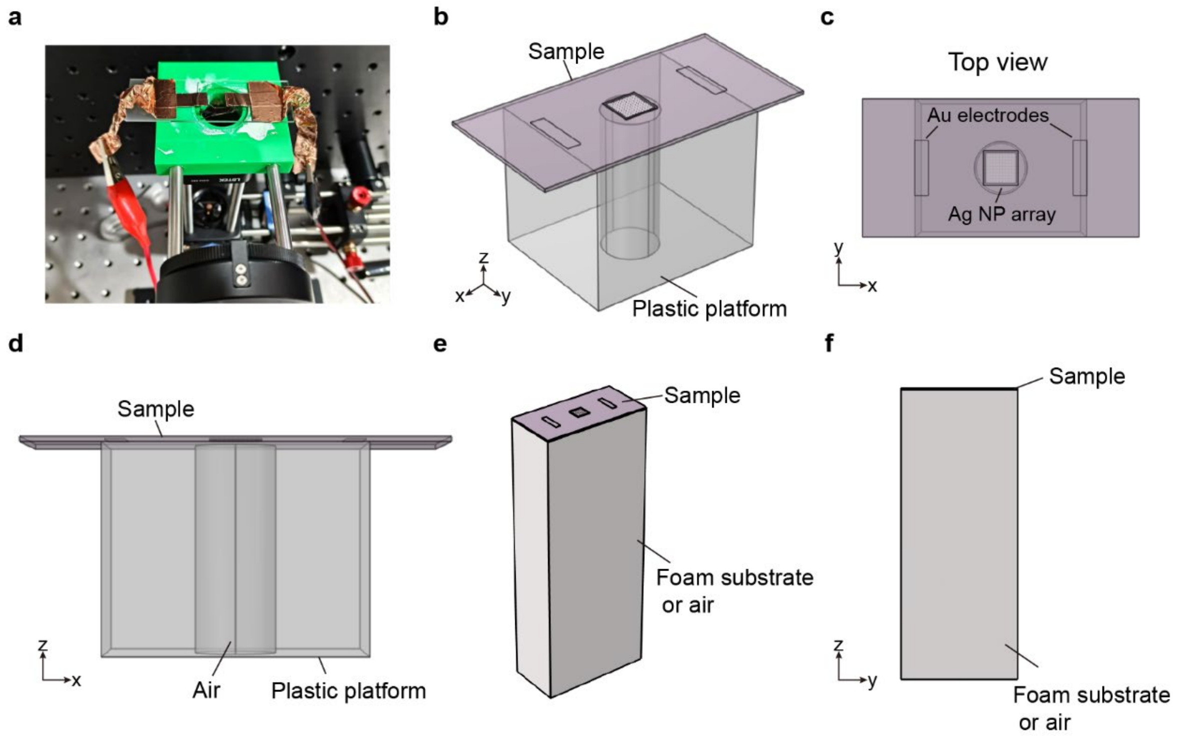

Figure S8. Modeling of samples placed on different substrates. (a) Photo of the experimental setup. **(b)** 3D model and **(c)** top view, and **(d)** XZ view of the sample on the plastic platform. **(e)** 3D model and **(f)** YZ view of the sample on the foam substrate or air.

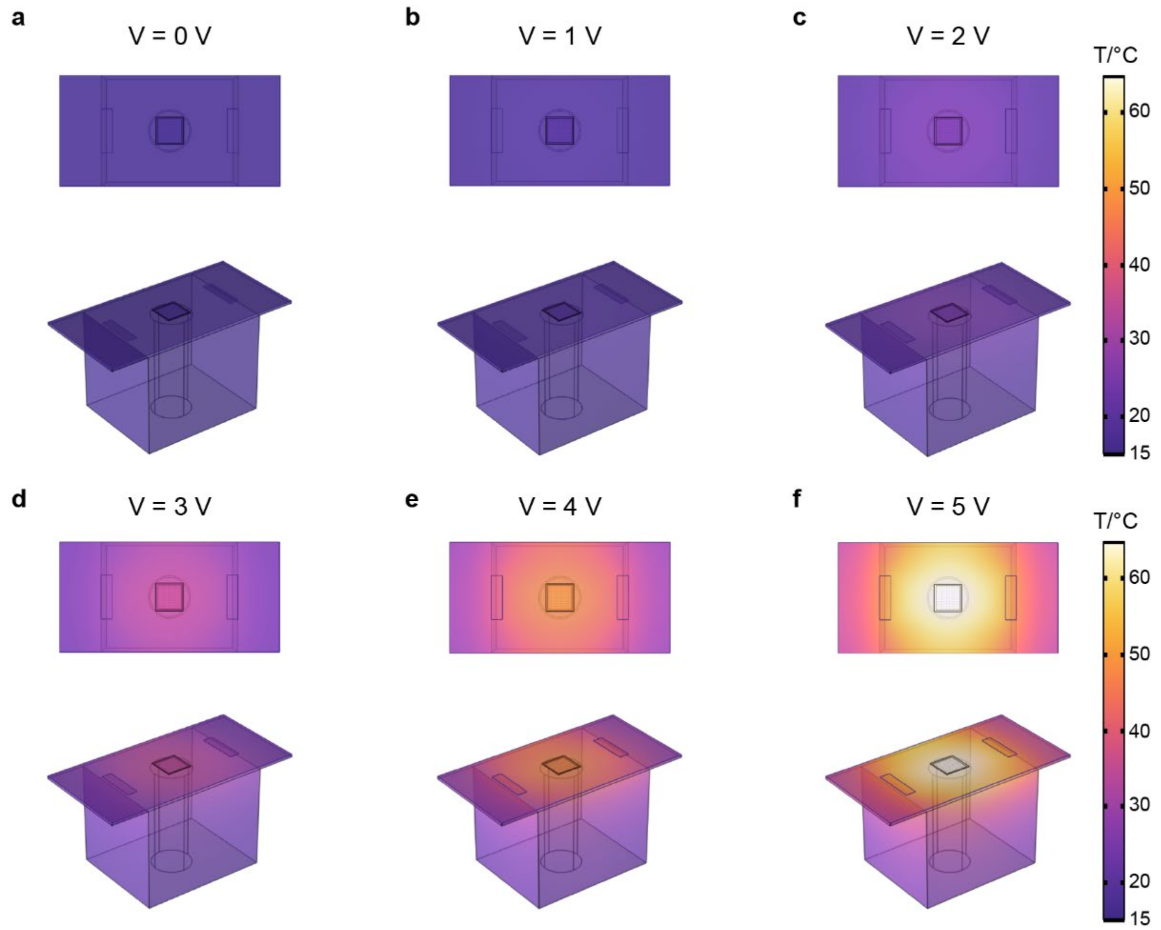

Figure S9 Simulated temperature distribution of the sample on the plastic platform with different voltages by COMSOL. Temperature distribution of the sample at **(a)** 0 V, **(b)** 1 V, **(c)** 2 V, **(d)** 3 V, **(e)** 4 V, and **(f)** 5 V.

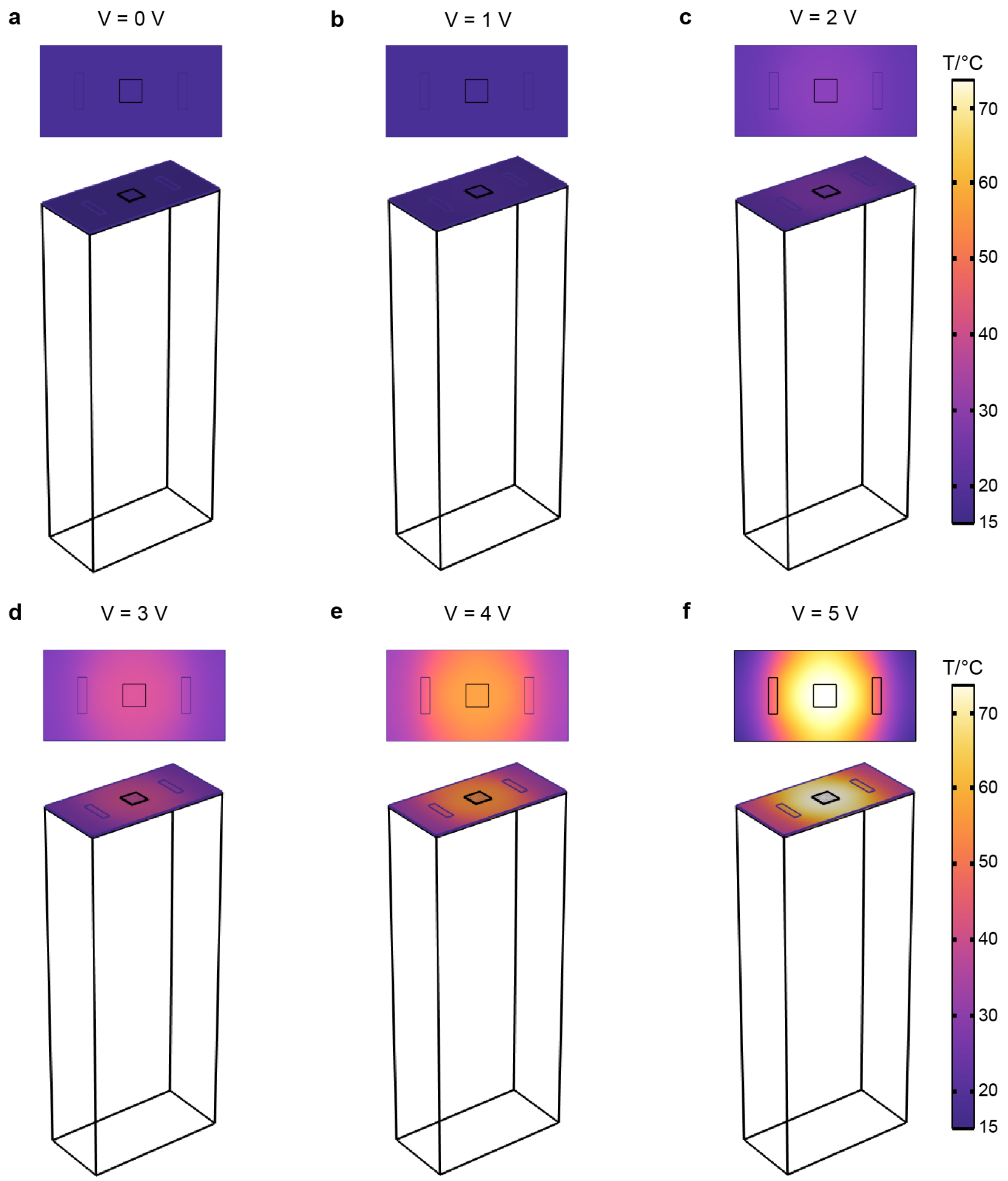

Figure S10. Simulated temperature distribution in air with different voltages by COMSOL. Temperature distribution of the sample at **(a)** 0 V, **(b)** 1 V, **(c)** 2 V, **(d)** 3 V, **(e)** 4 V, and **(f)** 5 V.

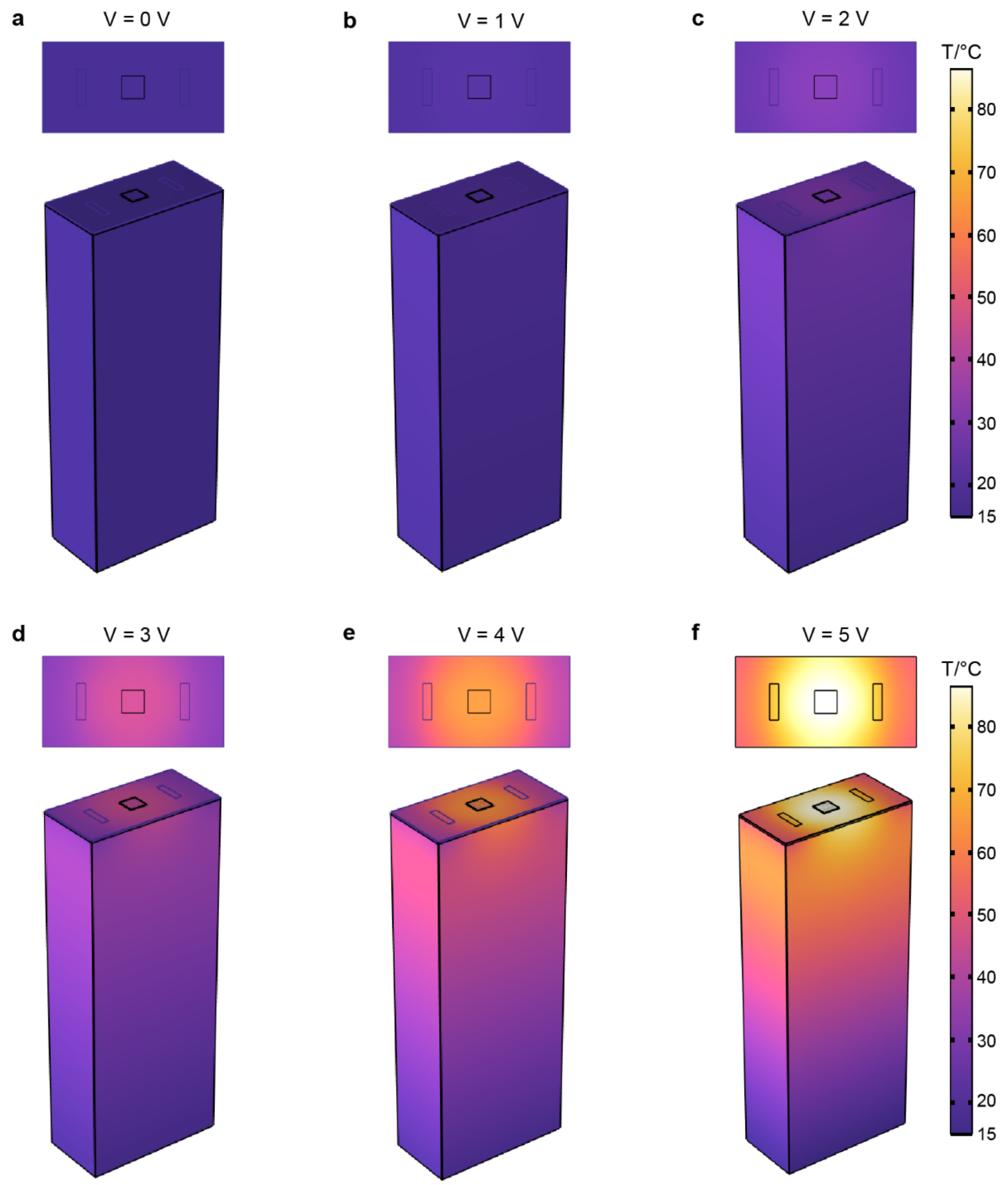

Figure S11. Simulated temperature distribution of the sample placed on the foam substrate at different voltages. Temperature distribution of the sample at **(a)** 0 V, **(b)** 1 V, **(c)** 2 V, **(d)** 3 V, **(e)** 4 V, and **(f)** 5 V.

The refractive index of DMSO at different temperatures measured by the Abbe refractometer

Table S2. RI of DMSO at different temperatures

Temperature (℃)	RI of the DMSO
10	1.4789
20	1.4755
30	1.4715
40	1.4681
50	1.4642
60	1.4598

We measured the refractive index of dimethyl sulfoxide (DMSO) at various temperatures using an Abbe refractometer. The maximum measurement temperature was limited to 60 °C, as the optical components of the Abbe refractometer may experience thermal expansion, which could result in inaccurate refractive index measurements.

The energy band and electric field distribution of the Ag metasurface

We present the energy band diagram for the Ag/ITO interface without the voltage. Here, E_0 and E_F denote the vacuum energy level and the unified Fermi level of Ag/ITO, respectively. E_C and E_V represent the conduction band edge and valence band edge energies of ITO, respectively. $q\varphi_{ITO}$ and $q\varphi_{Ag}$ denote the work function of the ITO and Ag, respectively.

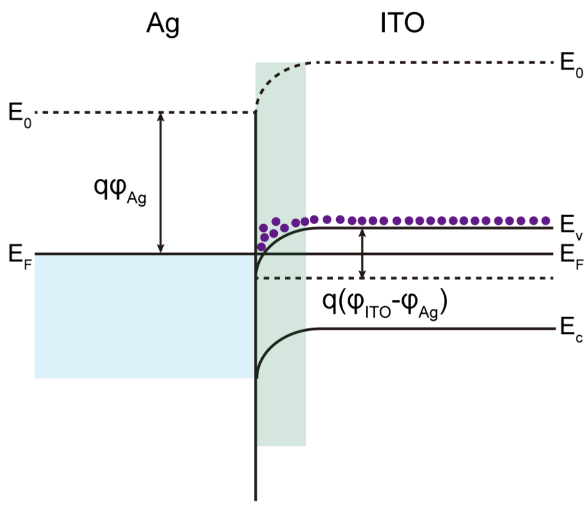

Figure S12. Energy band diagram of the Ag NP array and ITO layer without bias.

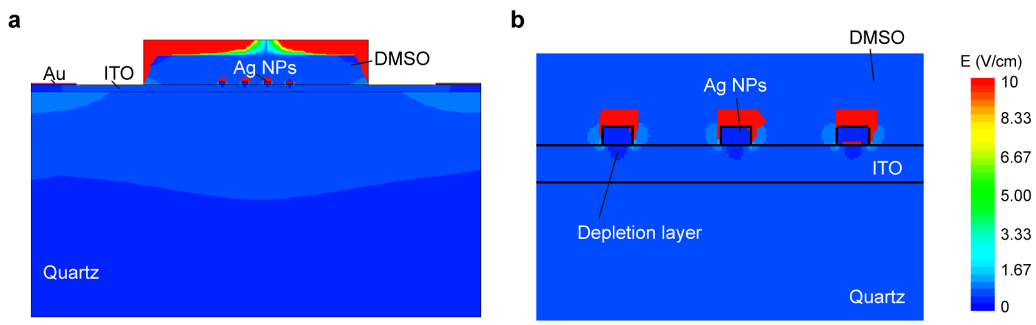

Figure S13. Simulated electric field distribution of the Ag metasurface. (a) Electric field of the Ag NP lattices on the ITGZO layer in the xz plane with a voltage of 5 V. **(b)** Magnified view of the interface between the Ag NPs and the ITO layer. A depletion layer forms between the Ag array and the ITO layer. Upon applying voltage, there is virtually no electric field along the z-direction between Ag and ITO, indicating minimal electron exchange between ITO and Ag.

We conducted a simulation to analyze the electric field distribution of the Ag metasurface in the xz plane after applying a 5V voltage. The results indicate that voltage application alone, without considering temperature, does not affect electron concentration in either the Ag (Al) or ITO (ITGZO) layers. Therefore, we propose that the electric field generated by the Seebeck effect results in localized variations in electron concentration within ITO. This phenomenon accounts for the greater experimental shift observed, which exceeds the predictions made by the simulation at the same temperature variation.

Simulated effect of Ag plasma frequency on transmission spectra

The optical resonance of Ag can be modeled by the Drude model, given by

$$\varepsilon_{Al} = \varepsilon_{inf} - \frac{{\omega_p}^2}{(\omega^2 + i\gamma\omega)}$$

Where ε_{inf} denotes the dielectric constant of metals at infinite frequency, ω_p and γ represent the plasma frequency and scattering frequency, respectively. The plasmonic resonance frequency of the metal can be expressed as:

$$\omega_p = \sqrt{\frac{Ne^2}{\varepsilon_0 m^*}}$$

The instinct plasmonic resonance frequency of Ag material is 1.37×10^{16} rad/s without the bias voltage, with $\varepsilon_{inf} = 3.7$, $\gamma = 0.24 \times 10^{14}\ rad/s$[3, 4]. To demonstrate the effect of increasing the electron concentration of Ag NPs surface on transmission spectral shifts, we simulated the transmission spectra at different plasmonic resonance frequencies ω_p of Ag NP ranging from 1.37×10^{16} rad/s to 1.4×10^{16} rad/s. A $\Delta\ \omega_p$ of 0.03×10^{16} rad/s results in a blue shift of ~ 2.3 nm for mode 1 and ~ 1.2 nm for mode 2, respectively.

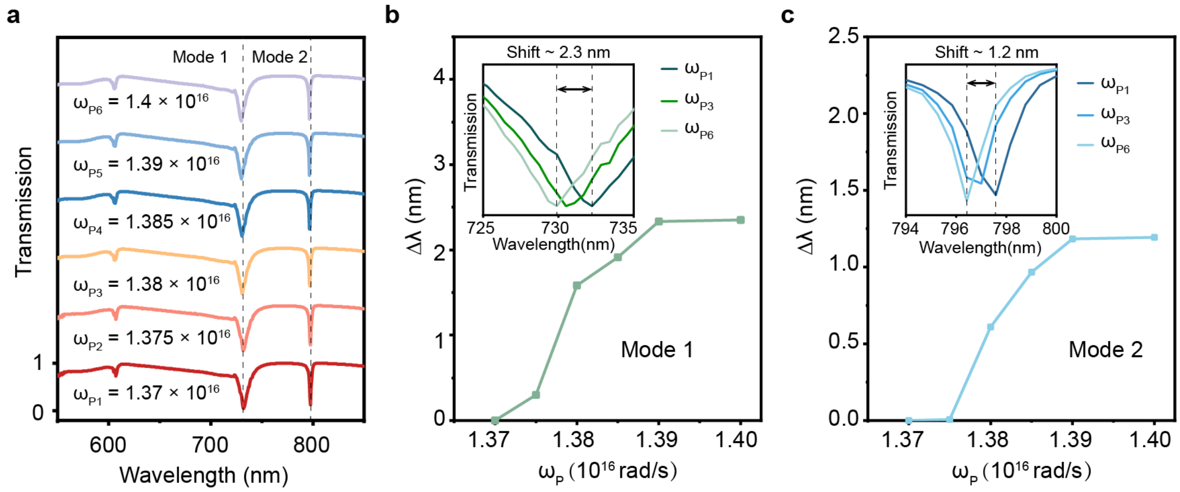

Figure S14. Simulated transmission spectra at different Ag plasma resonance frequencies. (a) Transmission spectra with Ag plasma resonance frequency from ω_{p1} to ω_{p6}. Wavelength shifts with the increase of ω_p in **(b)** mode 1. **(c)** mode 2. The insets in (b-c) show the shifts of transmission spectra in mode 1 and mode 2, with ω_{p1}, ω_{p3}, and ω_{p6}.

Simulated transmission spectra of the metasurface within the communication band by FDTD simulation

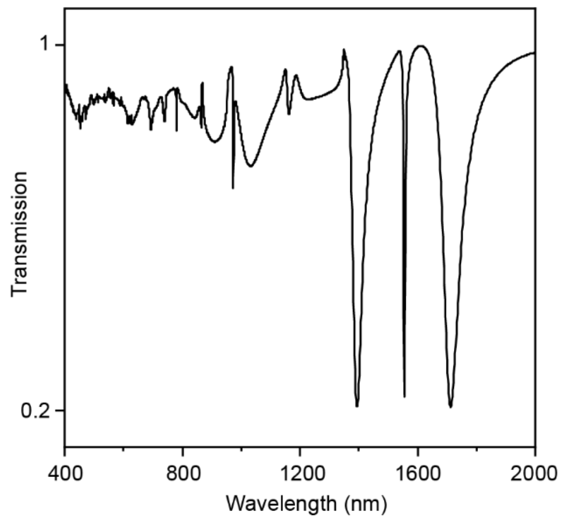

Figure S15. Simulated transmission spectra of the Ag metasurface within the communication band.

This electrically tunable metasurface can be equally suitable for the communication band. The metasurface is engineered with a transmission spectrum wavelength peak of 1550 nm, an Ag metasurface period of 950 nm, Ag NPs diameter of 300 nm, heights of 100 nm, and an ITO thickness of 150 nm.

Electrical modulation performance of the Al metasurface with the ITGZO layer

The period of the Al metasurface is 370 nm, the diameter of the Al NP is 80 nm, the height is 80 nm, and the thickness of the ITGZO is 150 nm, with Mode 1 at 548 nm, Mode 2 at 613 nm, and Mode 3 at 650 nm.

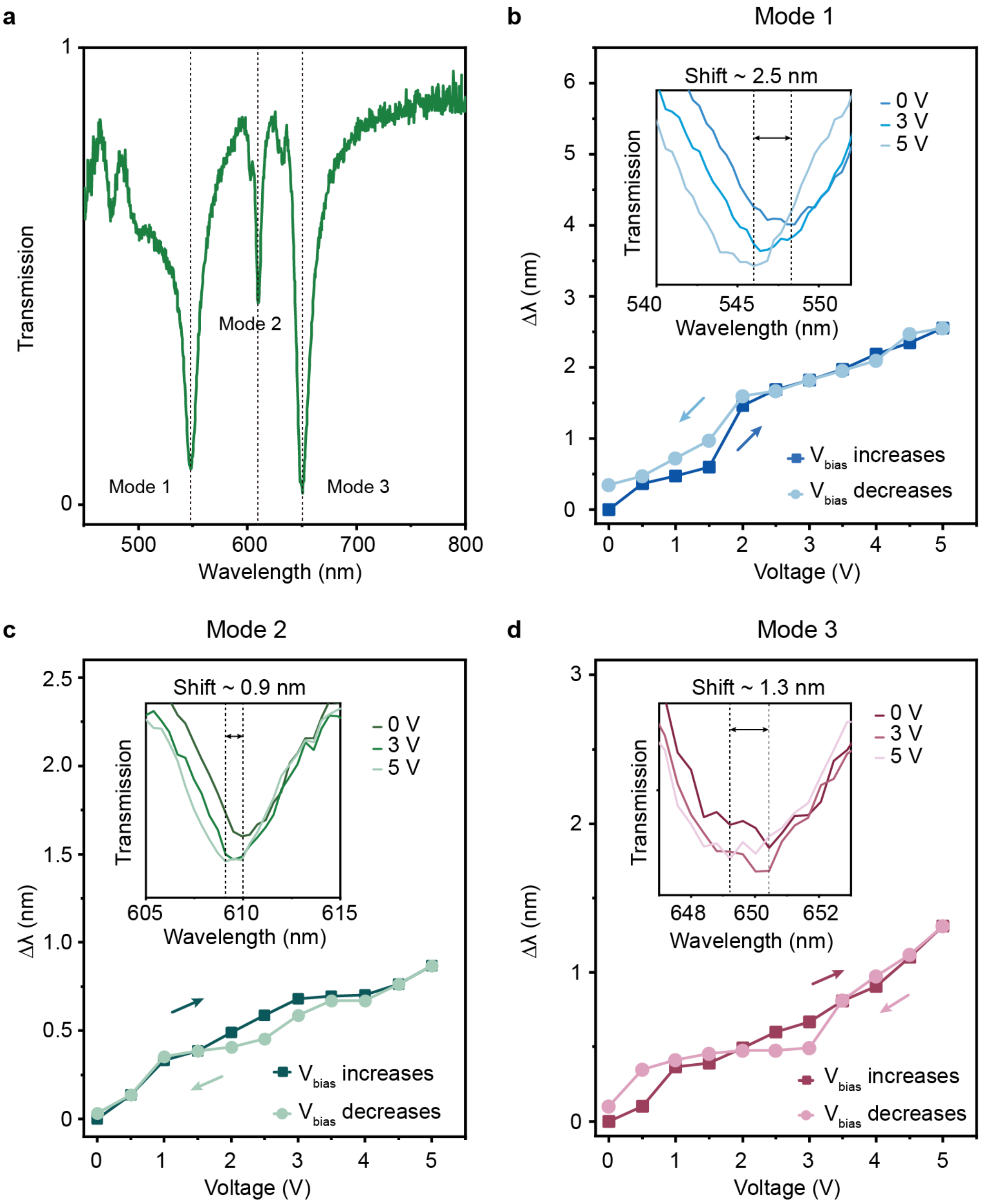

Figure S16. DC modulation performance of Al NP lattices with the ITGZO layer. (a) The experimental transmission spectra of Al metasurface. The variation of shifts with voltages from 0 V to 5 V of **(b)** mode 1, **(c)** mode 2, and **(d)** mode 3. The insets show the transmission spectra of mode 1, mode 2, and mode 3 at 0V, 3V, and 5V in (b-d). **(e)** Electrically modulated transmission spectra of the Al metasurface with bias voltages ranging from 0 V to 5 V. The variation of shifts with temperatures from 11 °C to 44 °C of **(f)** mode 1, **(c)** mode 2, and **(d)** mode 3.

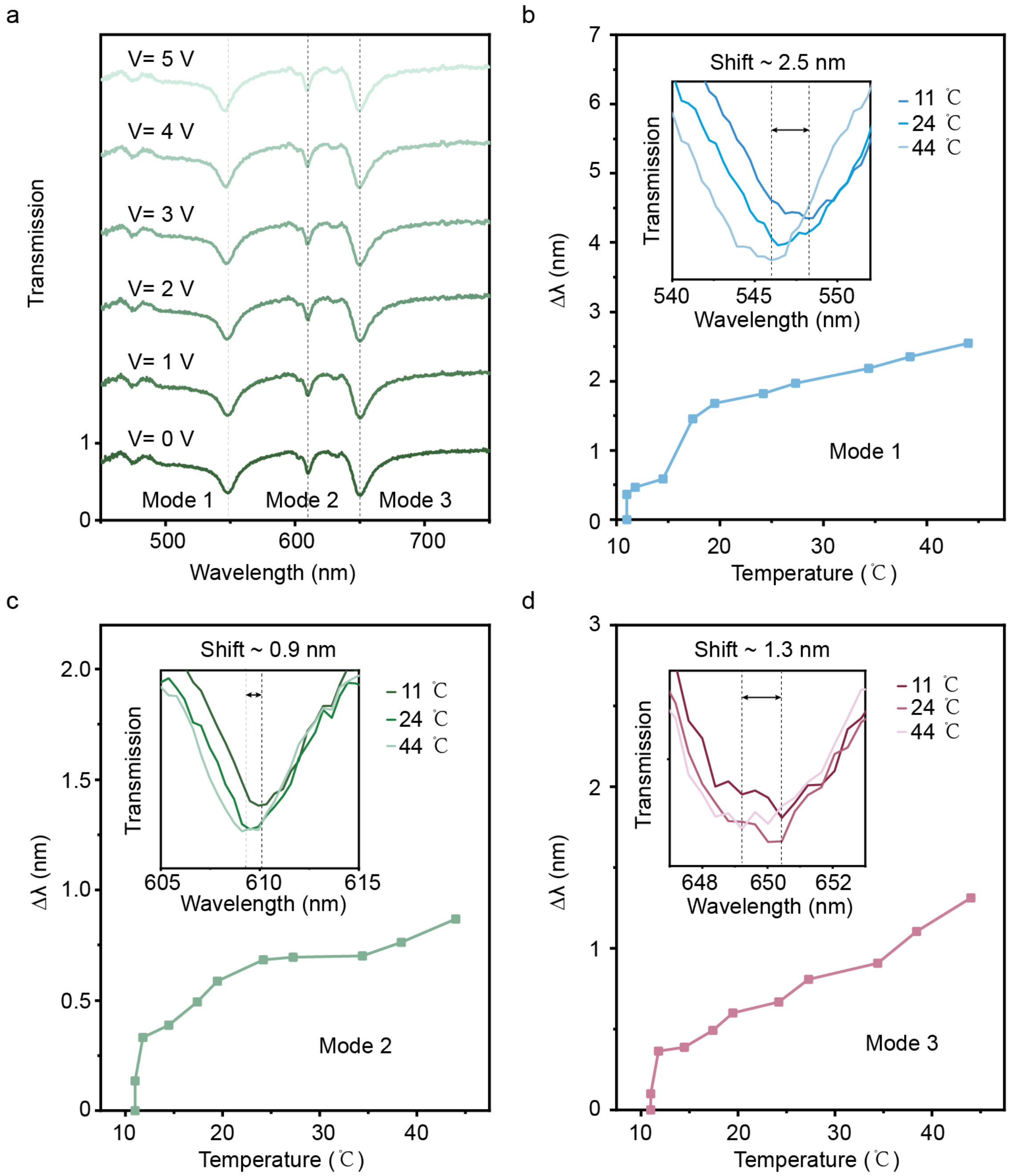

Figure S17. Electrical modulation performance of Al NP lattices with the ITGZO layer. (a) The experimental transmission spectra of Al metasurface at different voltages. The variation of shifts with temperatures from 11 °C to 44 °C of **(b)** mode 1, **(c)** mode 2, and **(d)** mode 3. The insets show the transmission spectra of mode 1, mode 2, and mode with the temperature of 11 °C, 24 °C, and 44 °C in (b-d).

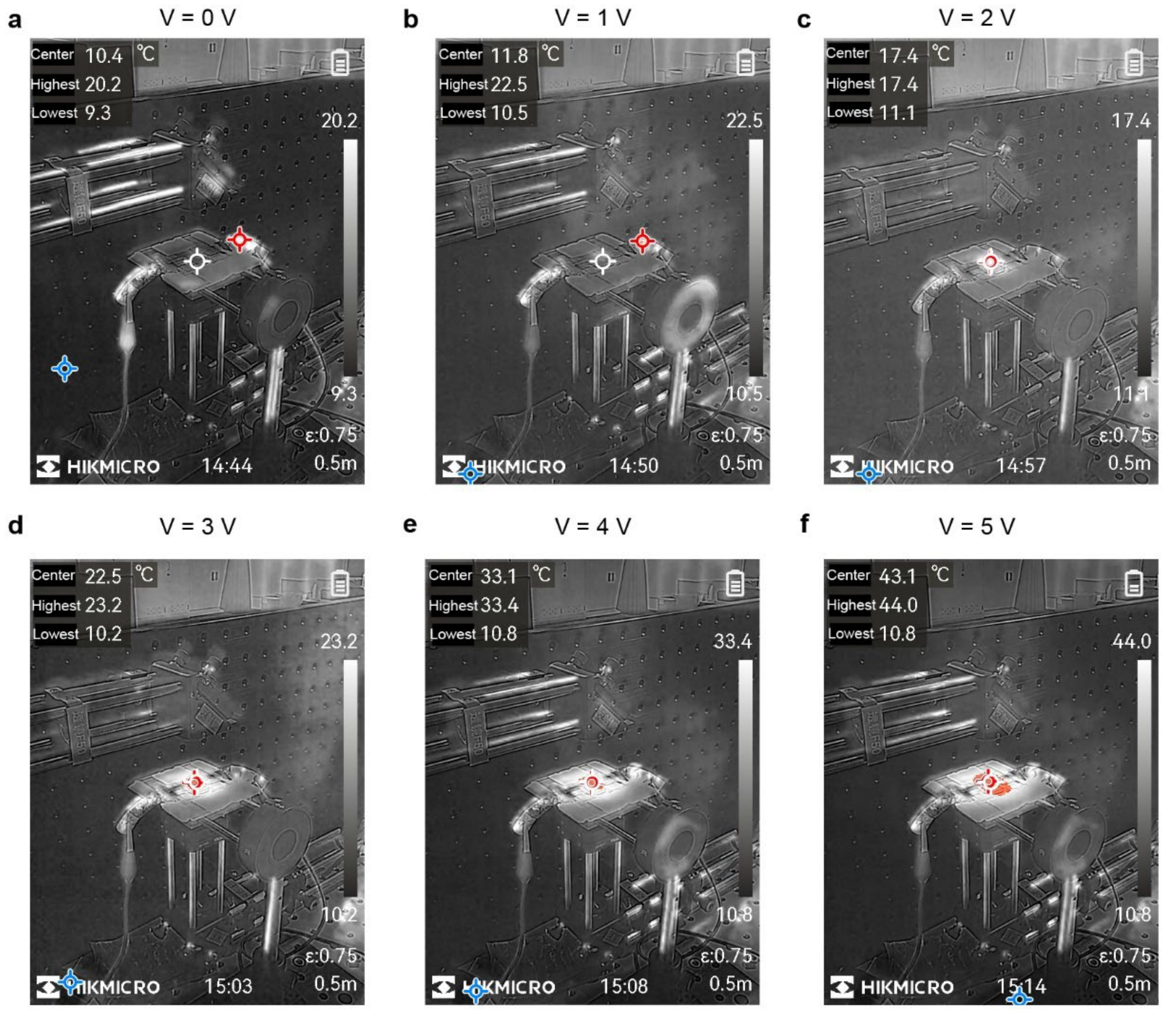

Figure S18. Temperature distribution of the Al metasurface at different voltages measured by the infrared thermal imaging camera. The white circle indicates the location of the sample, the blue circle indicates the area with the lowest temperature, and the red circle indicates the region with the highest temperature.

Simulated performance modulation in the Al metasurface

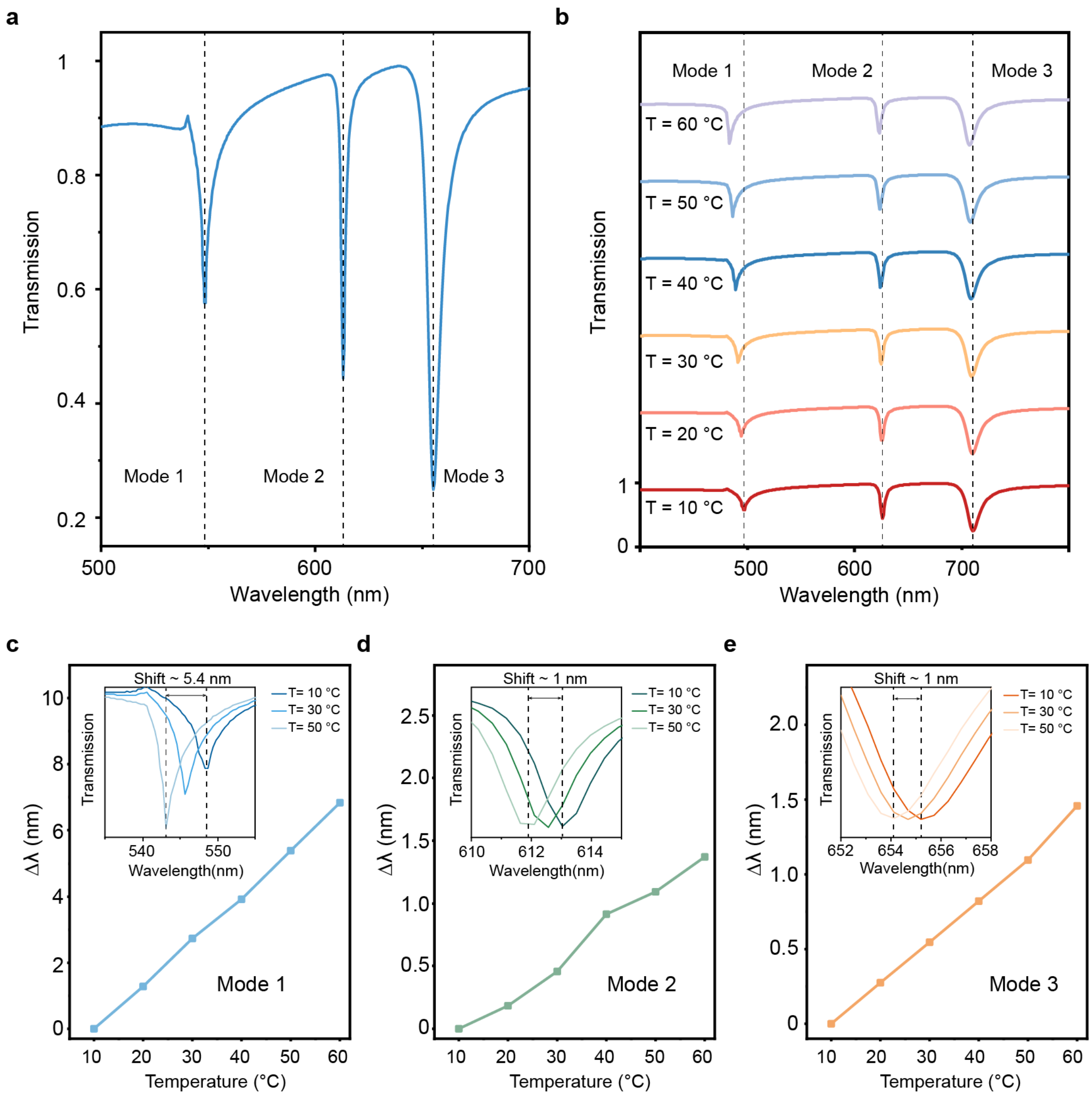

Figure S19. Simulated transmission spectra of the Al metasurface with different temperatures. (a) Simulated transmission spectra of the Al metasurface with 3 modes (gray dashed lines). **(b)** Simulated transmission spectra with temperatures varying from 10 ℃ to 60 ℃. The gray dashed lines label the initial wavelength peaks of three modes. The variation of shifts with temperature from 10 ℃ to 60 ℃ of **(c)** mode 1, **(d)** mode 2, and **(e)** mode 3.

The Al metasurface has a period of 370 nm, an Al NP diameter of 80 nm, a height of 80 nm, and an ITGZO thickness of 150 nm, with mode 1 at 541 nm, mode 2 at 611 nm, and mode 3 at 653 nm. All three modes exhibit blue shifts with the temperature ranging from 10 ℃ to 60 ℃, with distinct amounts of shifts. When the temperature was increased from 10 ℃ to 60 ℃, mode 1 exhibited a blue shift of ~ 5.4 nm, and modes 2 and 3 exhibited a blue shift of ~ 1 nm.

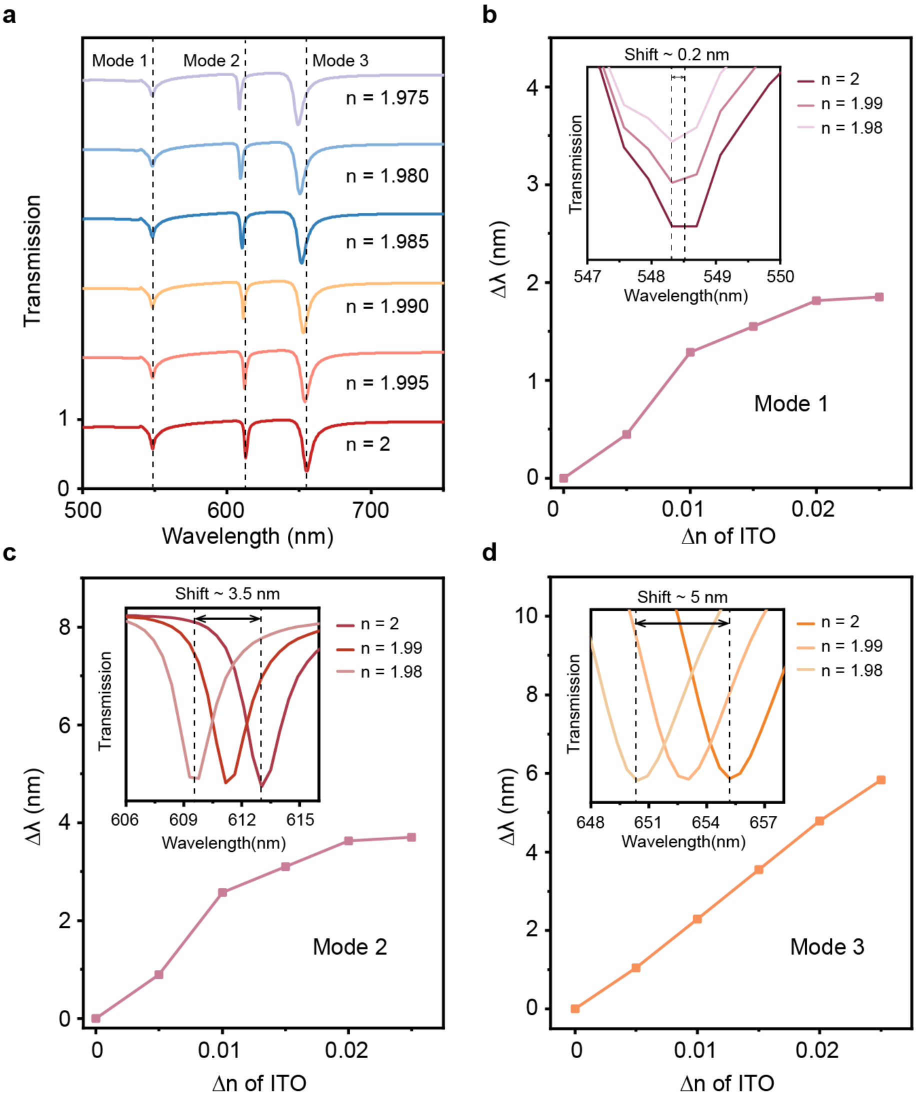

Figure S20. Simulated transmission spectra of the Al metasurface at different refractive indices of ITO. (a) Simulated transmission spectra with the refractive index of ITO varying from 2 to 1.97. The gray dashed lines label the initial wavelength peaks of three modes. The variation of shifts with Δ n from 0 to 0.025 of **(b)** mode 1, **(c)** mode 2, and **(d)** mode 3. The insets show the transmission spectra with the refractive index of ITO of 2, 1.99, and 1.98 of 3 modes in (b-d). The gray dashed lines show the largest shifts of the three modes.

The electrical modulation performance of the Al metasurface and the Ag metasurface with the ITO layer

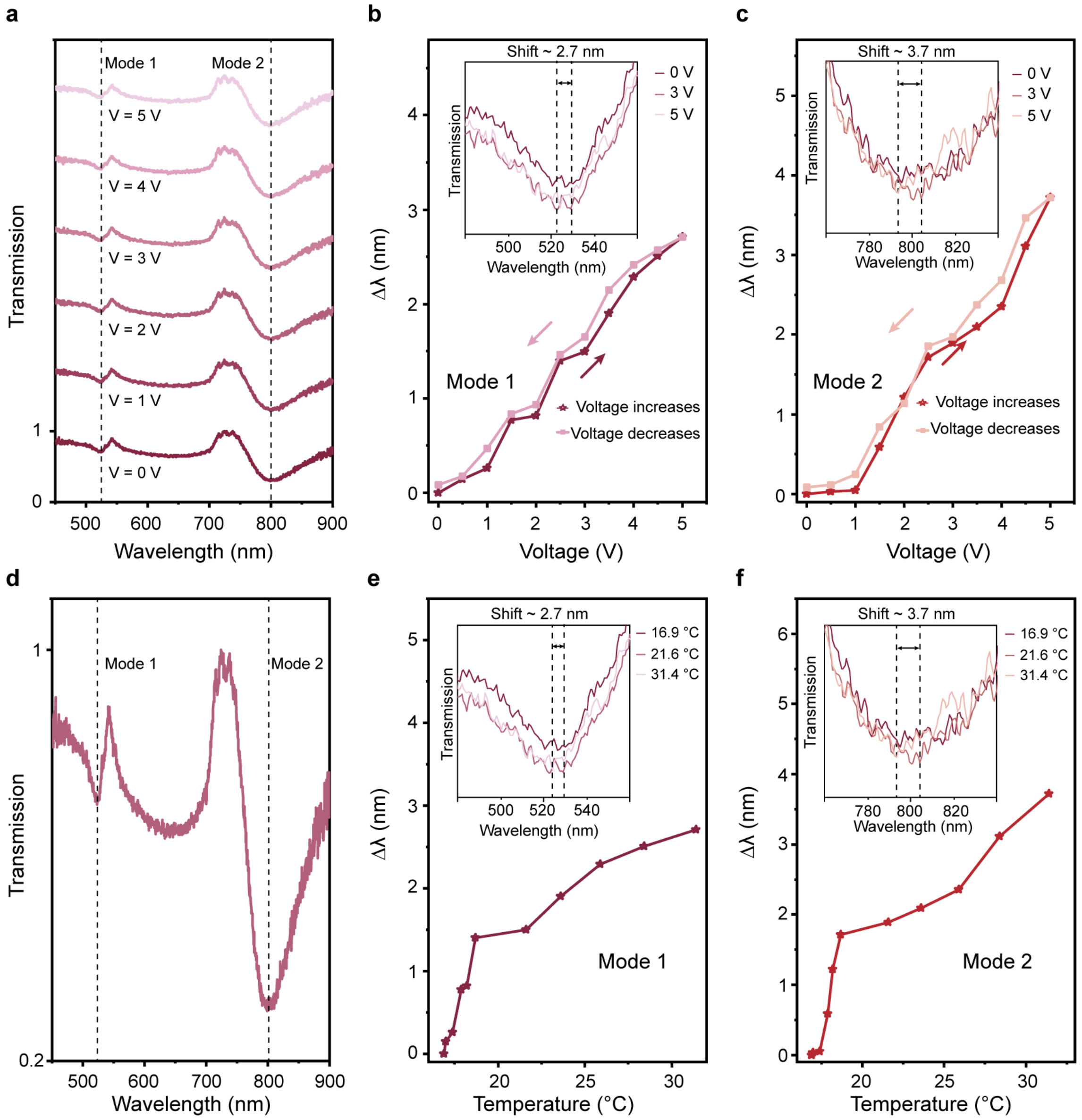

Figure S21. Electrical modulation performance of the Al metasurface with the ITO layer with period of 500 nm. (a) Electrically modulated transmission spectra of the Al metasurface with voltages from 0 V to 5V. The gray dashed lines label the wavelength peak of mode 1 and mode 2. Resonance shifts with the voltage increases (dark line) and the voltage decreases (light line) of **(b)** mode 1 and **(c)** mode 2. The inset in (b-c) shows the transmission spectra with the bias voltage of 0 V, 3 V, and 5 V. **(d)** Transmission spectra of the Al metasurface at 0 V with 2 modes (gray dashed lines). The variation of shifts with temperatures corresponding to the voltages from 16.9 ℃ to 31.4 ℃ of **(e)** mode 1 and **(f)** mode 2. The insets display the transmission spectra with the temperatures of 16.9 ℃, 21.6 ℃, and 31.4 ℃. The gray dashed lines show the largest shifts of the two modes.

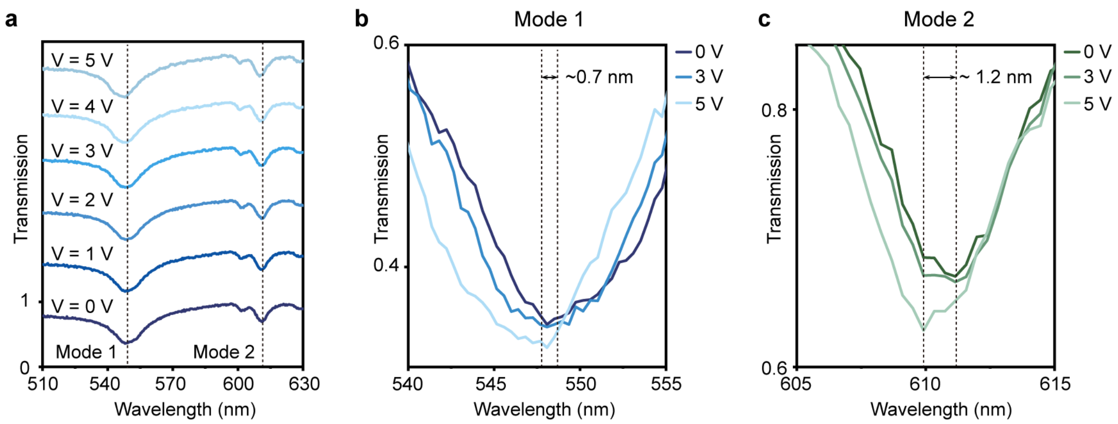

Figure S22. Electrical modulation performance of the Al metasurface on the ITO layer with a period of 370 nm. (a) Electrically modulated transmission spectra of the Al metasurface with voltages from 0 V to 5 V. The gray dashed lines label the wavelength peak of mode 1 and mode 2. The enlarged transmission spectra with the bias voltage of 0 V, 3 V, and 5 V of **(b)** mode 1 and **(c)** mode 2.

To further demonstrate the universality of electrical modulation in metasurfaces with varying geometries, we fabricated Al and Ag NP lattices with distinct lattice periods and NP sizes. The Al NP lattices with the ITO layer exhibit 2 resonance modes, characterized by a lattice period of 500 nm, an Al NP diameter of 150 nm, a height of 80nm, and an ITO thickness of 150 nm. The maximum wavelength shifts observed for two modes are ~ 2.7 nm and ~ 3.7 nm with the voltage ranging from 0 V to 5 V and temperature ranging from 16.9 °C to 31.4 °C. For an Al array with a period of 370 nm and a diameter and height of 80 nm, the wavelength shift is ~0.7 nm at 548 nm and 1.2 nm at 612 nm with a voltage of 5 V.

The Ag NP lattices with the ITO layer exhibit 2 resonance modes, with a lattice period of 500 nm, the diameter of Ag NP 150 nm, the height of 80nm, and the thickness of the ITO layer of 150 nm. The maximum wavelength shifts observed for two devices are ~ 4 nm and ~ 6 nm, with the voltage ranging from 0 V to 5 V and temperature ranging from 13 °C to 48 °C.

Shifts of all modes in these two metasurfaces exceed the temperature-induced shifts obtained by simulation, signifying the existence of electrical synergistic modulation.

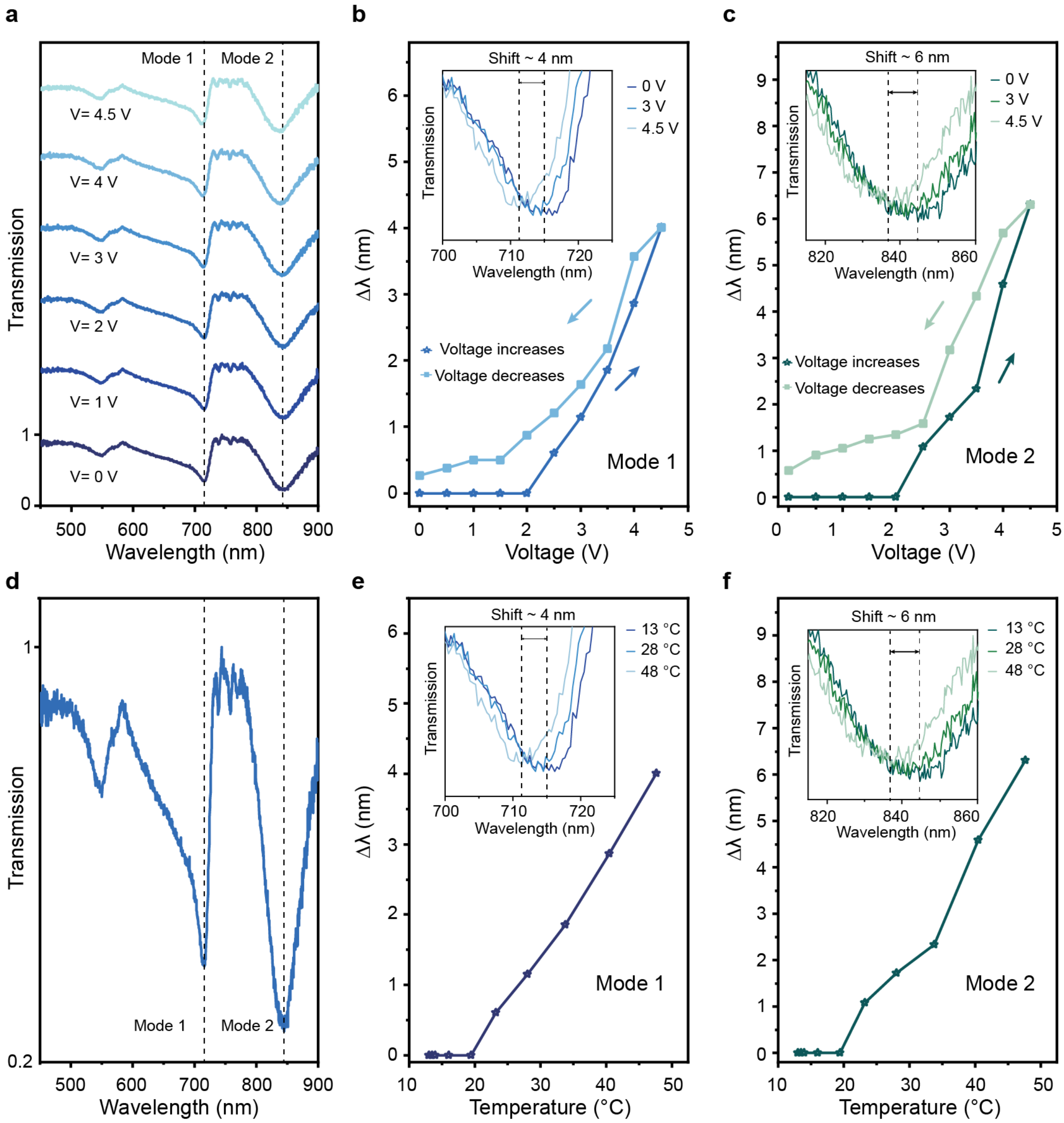

Figure S23. Electrical modulation performance of the Ag metasurface with the ITO layer. (a) Electrically modulated transmission spectra of the Ag metasurface with voltages from 0 V to 4.5V. The gray dashed lines label the wavelength peak of Mode 1 and Mode 2. Resonance shifts with the voltage increases (dark line) and the voltage decreases (light line) of **(b)** mode 1 and **(c)** mode 2. **(d)** Transmission spectra of the Ag metasurface at 0 V with 2 modes (gray dashed lines). The insets in (b-c) show the transmission spectra with the bias voltage of 0 V, 3 V, and 4.5 V. The variation of shifts with temperature variations corresponding to the voltages from 13 ℃ to 48 ℃ of **(e)** mode 1 and **(f)** mode 2. The insets display the transmission spectra at the temperatures of 13 ℃, 28 ℃, and 48 ℃. The gray dashed lines show the largest shifts of the two modes.

Electrical modulation performance of Ag NP lattices on the ITGZO layer at a wider voltage range.

We have added the transmission spectra with the operation voltages up to 12 V. At voltages exceeding 5 V, the resonance shift of Ag NPs on the ITGZO layer exhibits a linear relationship with the voltage. This increased wavelength shift is primarily attributed to the large temperature differential (approximately 50 °C) that occurs at these high voltages, which further reduces the refractive index of DMSO. And the variation in the refractive index of the TCO is further enhanced by the Seebeck effect. The observed broadening of the transmission spectrum at 10 V and 12 V may result from mismatched effective refractive indices with the substrate, potentially due to the evaporation or denaturation of DMSO. Further, high voltages can cause a rapid increase in temperature, leading to the evaporation or decomposition of DMSO. Therefore, proper encapsulation of DMSO at high voltages to prevent its evaporation can further improve the device performance.

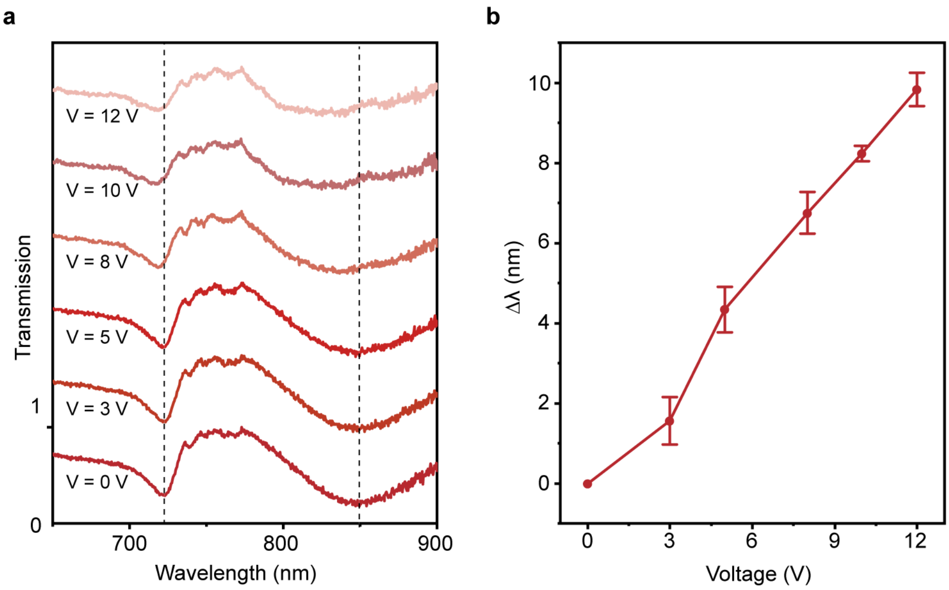

Figure S24. Electrical modulation performance of Ag NP lattices on the ITGZO layer. (a) Electrically modulated transmission spectra at 0 V, 3 V, 5V, 8 V, 10 V, and 12 V. (b) Wavelength shifts at 722 nm with the voltage increases.

Alternating Current (AC) modulation performance of the Ag metasurface

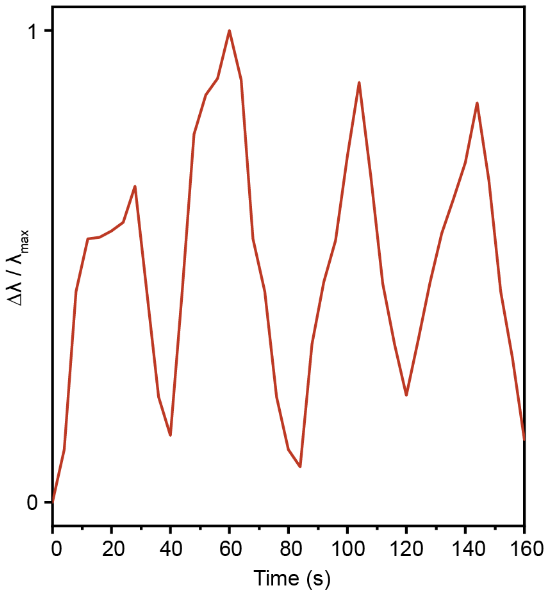

Figure S25. AC modulation performance of Ag NP lattices with ITGZO layer.

The signal generator we used produces a square wave signal with a value of peak-to-peak (VPP) of 4V and a period of 40s, with a rise time and a fall time of 20s each, and the spectrometer performs data acquisition every 4s for 200s.

The electrical modulation performance of the TiO_2 metasurface on ITGZO/quartz substrate

For dielectric metasurfaces, the reduction in DMSO refractive index upon voltage application, thereby causing a blue-shift of the resonant wavelength applies to dielectric metasurfaces. However, as the Seebeck effect occurs only in metals and semiconductors, it does not apply to the interface between the dielectric NP arrays and the TCO layer. We simulate a TiO_2 NP array with a period of 410 nm, a diameter of 130 nm, and a height of 80 nm, with a 150 nm thick layer of ITGZO. We mainly focus on the resonance wavelength of approximately 700 nm (**Figure S26**). As the temperature varies from 10 °C to 60 °C, the simulated transmission spectrum exhibits a continuous and pronounced blue shift, with the maximum shift of ~1.2 nm.

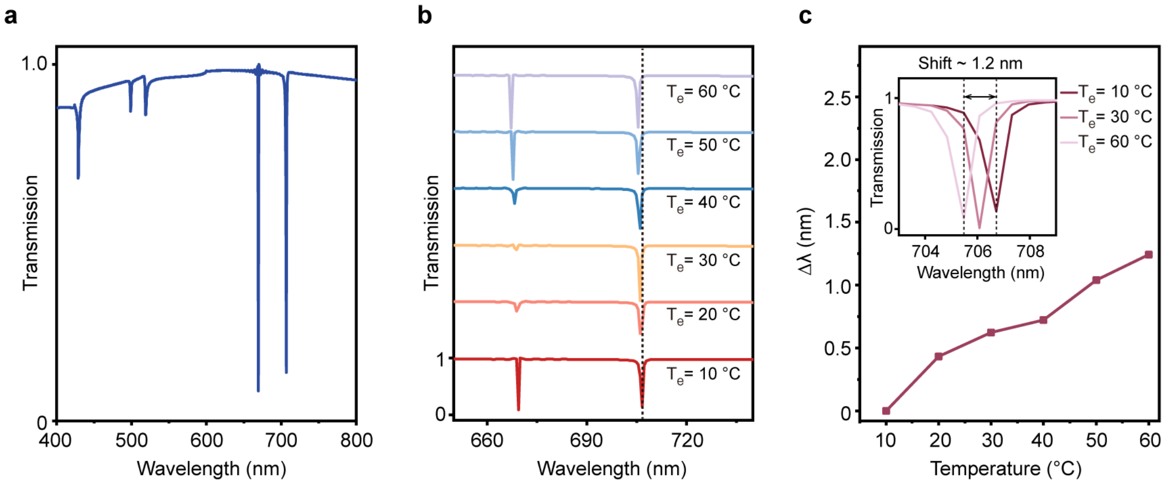

Figure S26. Simulated transmission spectra of TiO_2 metasurface. (a) Simulated transmission spectra of the TiO_2 metasurface. **(b)** Simulated transmission spectra with temperatures varying from 10 °C to 60 °C. The gray dashed lines label the initial wavelength peaks at ~700 nm. **(c)** The variation of shifts with temperature from 10 °C to 60 °C. The inset shows the resonance peaks at 10 °C, 30 °C, and 60 °C.

Further, we prepare a TiO_2 NP array with a period of 410 nm with the same device structure of metal NP lattices and measure the transmission spectra of TiO_2 at voltages varying from 0 V to 12 (**Figure S27**). The resonant wavelength at 720 nm with a linewidth of 2.5 nm exhibits a pronounced blue shift at 5 V, 10 V, and 12 V, with the maximum shift of approximately 0.75nm (**Figure S27 b-c**). This shift is in reasonable agreement with the wavelength shift observed in simulations under temperature variations of 30-40 °C. Using an infrared thermal imaging camera, we measured the temperature distribution of the sample at 0 V and 12 V, showing a temperature difference of approximately 30 °C.

Therefore, this supplementary experiment further demonstrates that the wavelength blue shift of the plasmonic metasurface induced by voltage application is caused by the change in both the refractive index of DMSO and the Seebeck effect at the metal-TCO interface.

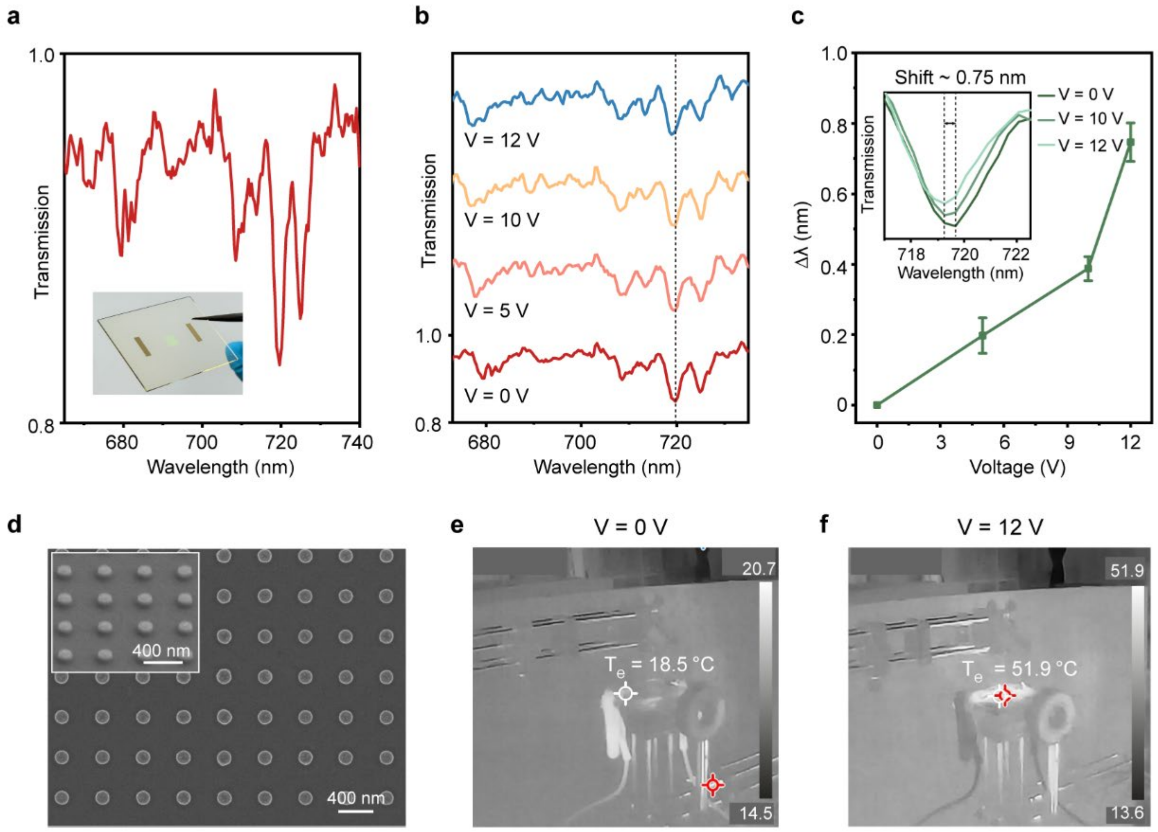

Figure S27. Electrical modulation of tunable metasurfaces composed of TiO_2 NP lattices on ITGZO layer. (a) Measured transmission spectra of TiO_2 NP lattices on ITGZO/quartz substrate. **(b)** Electrically modulated transmission spectra at 0 V, 5 V, 10 V, and 12 V. The grey dashed line indicates the resonant wavelength of interest. **(c)** Resonance shifts of Ag NP lattices on ITO with the voltage increases. The inset shows the resonance peaks with bias voltages of 0 V, 10 V, and 12 V. **(d)** SEM image of the top view of TiO_2 NP lattices. The inset shows the SEM image at a 45-degree angle of TiO_2 NP lattices. The temperature distribution at **(e)** 0 V and **(f)** 12 V measured by the infrared thermal imaging camera.

Photo of the experiment setup for characterization of the electrical modulation performance of metasurfaces.

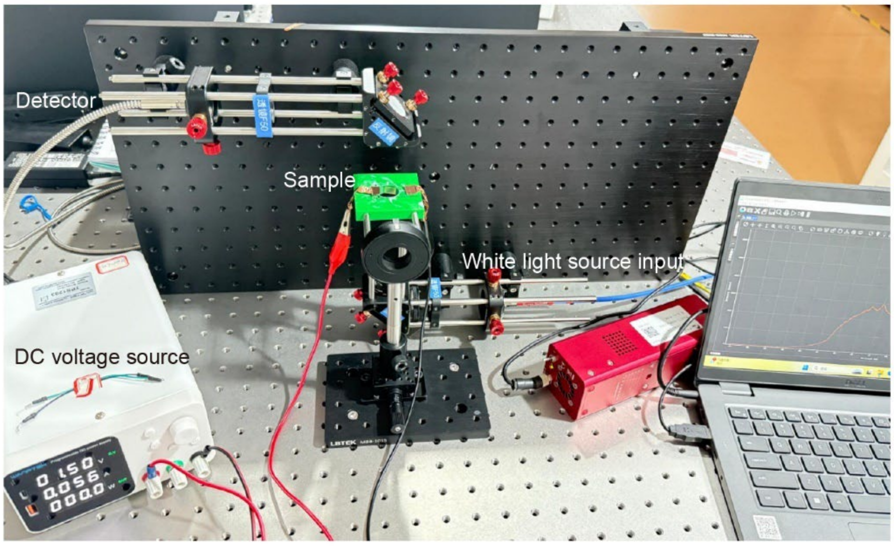

Figure S28. Experiment setup for characterization of direct current (DC) performance.

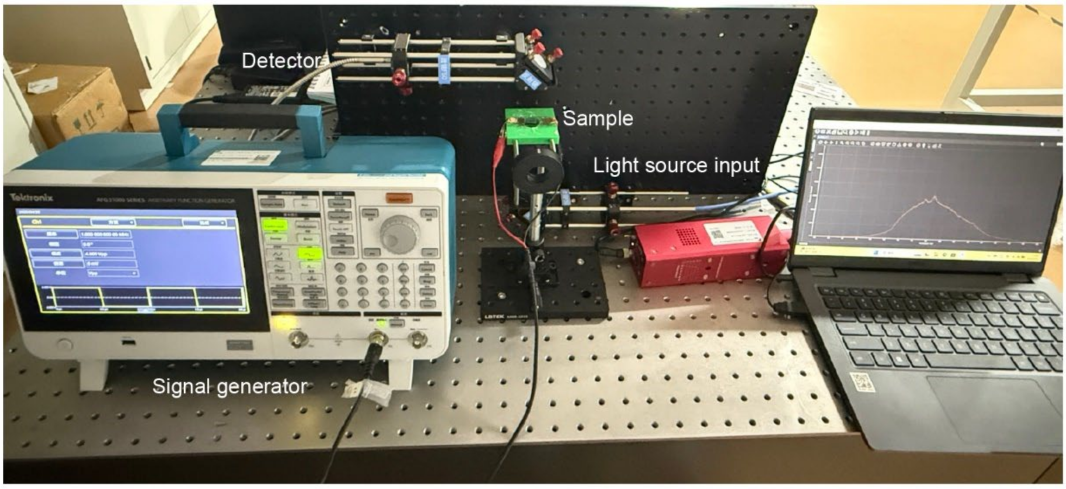

Figure S29. Experiment setup for characterization of AC performance and image transmissions.

References

1. Lee MH, Huntington MD, Zhou W, Yang J-C, Odom TW. Programmable Soft Lithography: Solvent-Assisted Nanoscale Embossing. *Nano Letters* **11**, 311-315 (2011).

2. Kogelnik H. Theory of Optical Waveguides. In: *Guided-Wave Optoelectronics* (ed Tamir T). Springer Berlin Heidelberg (1988).

3. Mock JJ, Barbic M, Smith DR, Schultz DA, Schultz S. Shape effects in plasmon resonance of individual colloidal silver nanoparticles. *The Journal of Chemical Physics* **116**, 6755-6759 (2002).

4. Palik, Edward D. Handbook of optical constants of solids. *Academic Press*, (1985).